PHYSICAL REVIEW B **98**, 041114(R) (2018)

Rapid Communications

Planar Hall effect in the type-II Weyl semimetal T_d-MoTe$_2$

F. C. Chen,[1,2] X. Luo,[1,*] J. Yan,[1,2] Y. Sun,[3] H. Y. Lv,[1] W. J. Lu,[1] C. Y. Xi,[3] P. Tong,[1] Z. G. Sheng,[3,4]
X. B. Zhu,[1] W. H. Song,[1] and Y. P. Sun[1,3,4,†]

[1] *Key Laboratory of Materials Physics, Institute of Solid State Physics, Chinese Academy of Sciences, Hefei 230031, China*
[2] *University of Science and Technology of China, Hefei 230026, China*
[3] *High Magnetic Field Laboratory, Chinese Academy of Sciences, Hefei 230031, China*
[4] *Collaborative Innovation Center of Advanced Microstructures, Nanjing University, Nanjing 210093, China*

(Received 22 May 2018; revised manuscript received 28 June 2018; published 30 July 2018)

Topological Weyl semimetals (WSMs), a new quantum state of matter, provide the realization of relativistic Weyl fermions in solid-state physics. The appearance of the Weyl nodes will demonstrate novel transport phenomena related to the chiral anomaly. Theoretical prediction hints that the giant planar Hall effect (PHE) can be induced by the chiral anomaly in the WSMs. In this work, we performed PHE measurements to probe chiral charge in type-II WSM T_d-MoTe$_2$. Robust transverse voltage can be acquired when the magnetic field and electric current is coplanar. Subsequently, the amplitude of intrinsic PHE increased sharply at $T = 50$ K with the decreasing temperature. The increasing trend in the temperature dependence is attributed to coupling effect between the chiral charge and the electric one, which drives the system into intermediate-coupling states at higher field. Our work confirms that the PHE measurement is a practical transport tool to probe chiral charge pumping effect in the WSMs systems.

DOI: 10.1103/PhysRevB.98.041114

The discovery of the topological Weyl semimetals (WSMs) has sparked enormous research interests recently since it provides the realization of the Weyl fermions in condensed-matter physics [1,2]. The WSMs can be classified into two types: In the type-I WSMs, the linear nondegenerate bands cross at the Weyl points (WPs), leading to a pointlike Fermi surface (FS) if the chemical potential is tuned to the energy of WPs; however, the type-II WSMs break the Lorentz symmetry, and the hole and electron pockets, which form the WPs [1,2], overlap over a range of energies, leaving a finite density of states at the chemical potential [3–5]. Above all, one of the most distinct properties of WSMs is the existence of nonconservation of chiral charge induced by parallel electric and magnetic fields. In this situation, the generation of the electric current or the negative magnetoresistance (MR) can be realized in the presence of parallel electric and magnetic fields [6,7]. It also connects the transport feature in solid-state physics with the physics of relativistic fermions. Recently, the planar Hall effect (PHE)–the giant transverse voltage can be demonstrated in the case of coplanar electric and magnetic fields ($\boldsymbol{E}\cdot\boldsymbol{B} = EB\cos\theta, \theta \neq 0, \pi/2$)–was initially observed in ferromagnetic materials and has been predicted to be another fingerprint feature of the chiral charge in topological semimetals (TSMs) [8,9]. When the separated Weyl nodes are subjected to the electric field E and magnetic field B, the key feature is that the chiral current is pumped between the nondegenerate points and the current is along the magnetic field, which leads to the anisotropy of the magnetotransport driven by chiral anomaly. The off-diagonal part of the resistivity represents the PHE based on the chiral current and is mainly caused by the chiral anomaly and the Lorentz force [8–12]. It is a macroscopic manifestation of the quantum anomaly in relativistic field theory of chiral fermions. Theoretically, the PHE in nonmagnetic TSMs can be attributed to the nontrivial Berry curvature and chiral anomaly. Experimentally, the PHE has been observed in several Dirac semimetals such as Cd$_3$As$_2$ and ZrTe$_5$, which provides a direct relationship between the physics of topological nature and the transport properties [10–12].

Among the type-II WSMs, T_d-MoTe$_2$ is a typical example. MoTe$_2$ crystallizes in several different polytypes: the semiconducting $2H$ phase, the centrosymmetric $1T'$ phase, and the noncentrosymmetric T_d phase [13–15]. The semiconducting $2H$ structure has been studied extensively for electronic and optoelectronic device applications [13]. For the metallic $1T'$ and T_d structures, when the $1T'$ phase is cooled it undergoes a structural transition at 240 K to become T_d phase [16]. Moreover, many interesting properties such as extremely large magnetoresistance and superconductivity have been demonstrated in T_d-MoTe$_2$ [17–19]. Another fascinating feature of T_d-MoTe$_2$ is the existence of topological Weyl node. Theoretical works reported that the observed electron and holes pockets touch each other at eight WPs, in which some of the WPs located in the vicinity of the Fermi level while the other type is far from the Fermi level [20,21]. Angle-resolved photoemission spectroscopy and scanning tunneling microscopy/spectroscopy (STM/STS) provided direct evidence of topological Fermi arc at the boundary of electron and holes pockets and the existence of surface state [3–5,22]. While spectroscopy measurements have identified the character of WPs in T_d-MoTe$_2$, evidence extracted from the transport experiments for the existence of chiral fermions has been lacking currently [7,22–25]. Moreover, the interference

---

[*] Corresponding author: xluo@issp.ac.cn
[†] Corresponding author: ypsun@issp.ac.cn

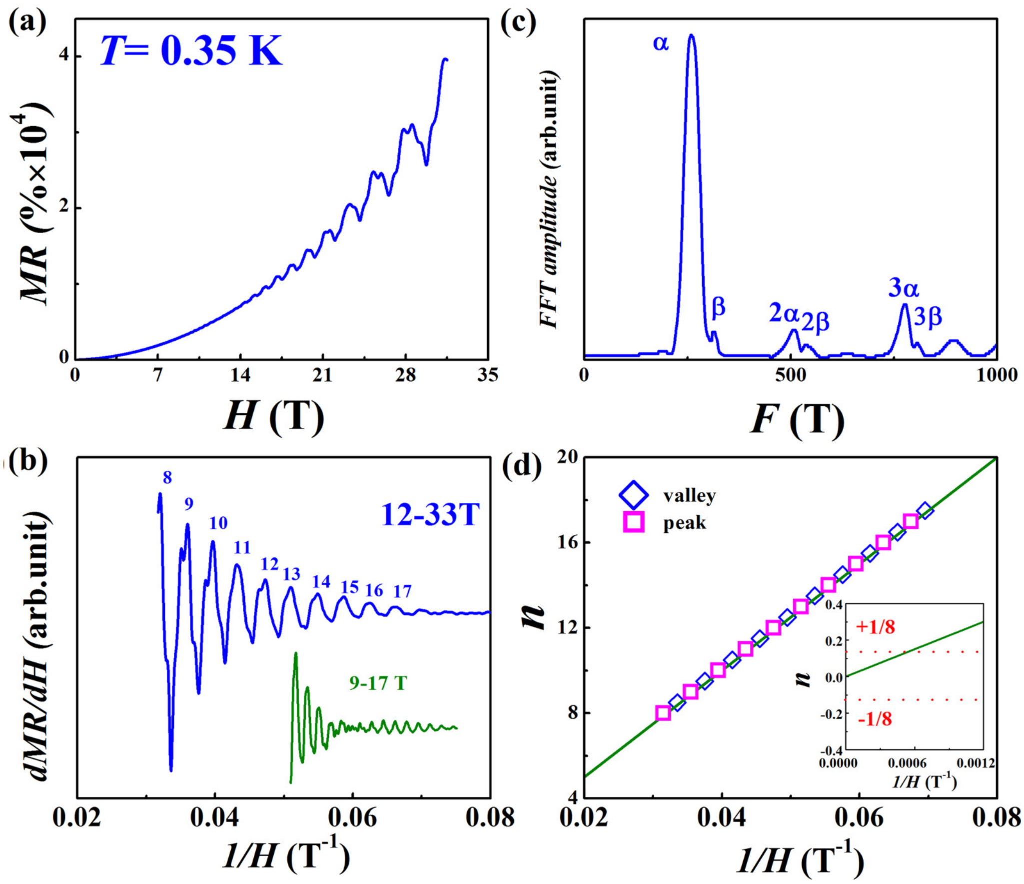

FIG. 1. (a) The magnetoresistance of T_d-MoTe$_2$ with $H \parallel c$ and $I \parallel a$, measured at 0.35 K; (b) Shubnikov–de Haas oscillations component dMR/dH as a function of inverse magnetic field. Data are normalized and shifted for clarity; (c) the FFT spectra; and (d) Landau level index n plotted against $1/H$ for the α pocket, and the pink (blue) open symbol indicate integer (half integer) index (the peak (valley) of dMR/dH). The inset shows the intercept lying between $\pm 1/8$, which is a strong piece of evidence for a nontrivial Berry phase.

of the trivial crossing bands and the large energy separation between the WPs prevents us from observing the negative MR effect in T_d-MoTe$_2$ [20,21]. Another tool to determine the chiral anomaly in T_d-MoTe$_2$ is really needed. In this work, we demonstrate the observation of the chiral-anomaly-induced PHE in T_d-MoTe$_2$ single crystal. At first, the nontrivial Berry phase was obtained from the Shubnikov–de Haas oscillation result. After subtracting the MR components originating from the experimental misalignments, we tracked the signature of chiral anomaly–the obtained PHE resistance displays an $\sim \cos\theta\ \sin\theta$ dependence, which is consistent with the theoretical prediction. We also present that the band reconstruction, emerging at $T = 50$ K, strengthens the coupling between the trivial electric and chiral charge and amplifies the PHE at lower temperature. The different coupling states induced by FS reconstruction have also been discussed. Our conclusions not only pave a way to further recognize the exotic features of chiral anomaly in T_d-MoTe$_2$, but also shed light on the discovery of chiral charge in other systems.

$1T'$-MoTe$_2$ single crystals were grown by the flux method using Te as solvent. The crystal growth recipe is followed from the reported paper. The experimental and calculated details can be found in the Supplemental Material [26].

Whereas both the theoretical prediction and spectroscopy measurements indicate the existence of Weyl nodes in T_d-MoTe$_2$, measurement of quantum oscillations is a very powerful way to probe the nontrivial Berry phase acquired by the WSMs [27]. Thus we present the field dependence of MR for T_d-MoTe$_2$ at $T = 0.35$ K in Fig. 1(a). A magnetic field was applied from 0 T up to 33 T. After subtracting the background by using polynomial fits, clear oscillation patterns are presented in Fig. 1(b). According to the Lifshitz-Onsager quantization rule, the Landau index n is linearly dependent on $1/H : \hbar S_n/2\pi eH = n - \gamma + \delta$; here γ is the Onsager phase factor which is related to the Barry phase through $\gamma = 1/2 - \phi_B/2\pi$ and the value of δ changes from 0 for a quasi-two-dimensional cylindrical FS to $\pm 1/8$ for a corrugated FS [27,28]. For a conventional metal with trivial parabolic dispersion, the Berry phase $\phi_B = 0$, hence $\gamma = 1/2$. However, for a system with linear band dispersion, the nontrivial Berry phase $\phi_B = \pi$ that makes $\gamma = 0$. The fast Fourier transform (FFT) pattern is similar with the reported one [29]. We assign the peak positions as the Landau integer indices and the valley positions as the half indices. Figure 1(d) shows the linear extrapolation of $1/H$ versus the integer n plot, in which $\gamma - \delta$ locates between $0 \pm 1/8$. Here, the zero Onsager phase corresponds to a nontrivial Berry phase, which provides strong evidence for the existence of Weyl fermions in T_d-MoTe$_2$.

We now proceed to explore the chiral-anomaly-induced giant PHE and other intriguing electronic properties of this

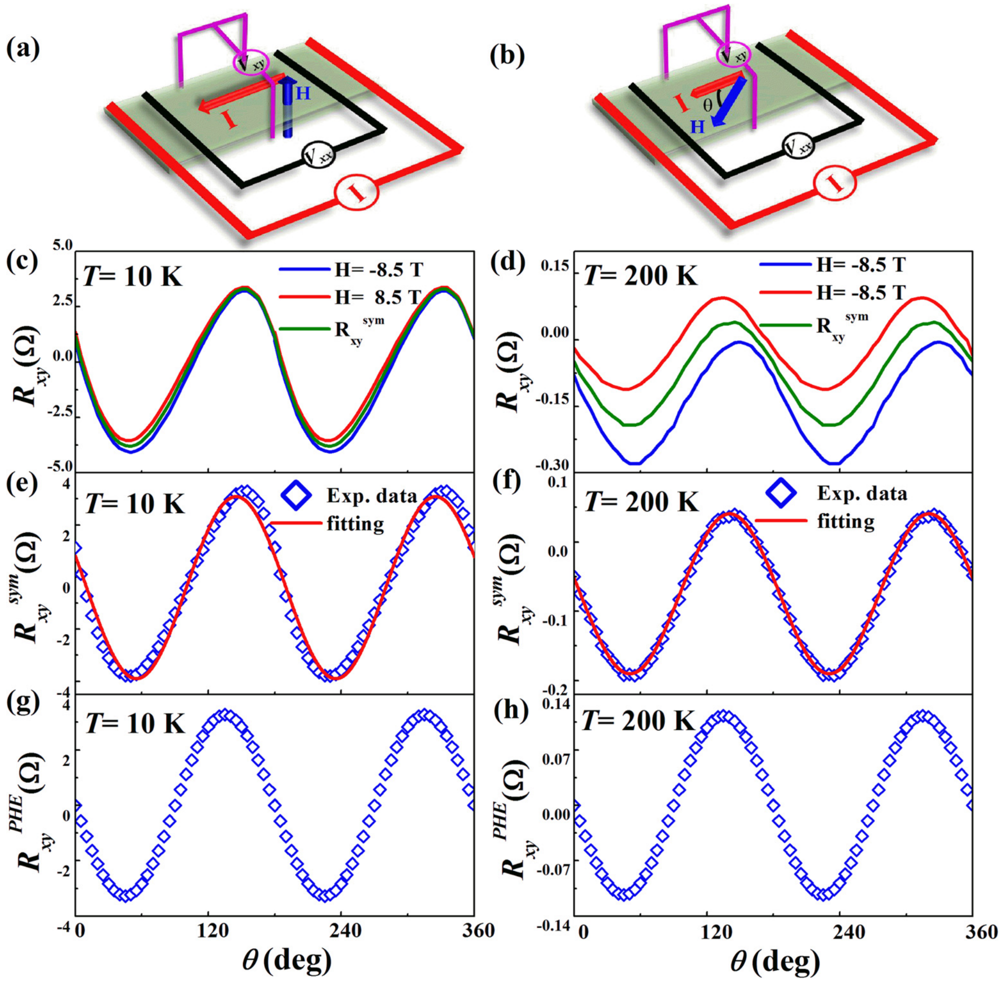

FIG. 2. (a) and (b) Schematic illustrations for the usual and planar Hall measurement configurations. (c) and (d) The planar Hall resistance with $H = \pm 8.5\,\mathrm{T}$ at $T = 10$ and 200 K, respectively. (e) and (f) The average planar Hall resistance at $T = 10\,\mathrm{K}$ and 200 K, respectively. Open symbols are the experimental data while red lines are the fitting results. (g) and (h) The intrinsic planar Hall resistance at $H = 8.5\,\mathrm{T}$ after subtracting the misalignment components.

material. Figure 2(a) shows the schematic diagram of a usual Hall experimental setup, in which the magnetic field H always lies perpendicular to the sample plane. However, in our PHE measurement setup shown in Fig. 2(b), the voltage and the current are same with the case of usual Hall configuration while H is applied and rotated in the sample plane with an angle θ to the current direction. Figures 2(c) and 2(d) illustrate the angular dependence of the planar Hall resistance of T_d-MoTe$_2$ with $H = \pm 8.5\,\mathrm{T}$, at $T = 10$ and 200 K, respectively. Due to the misalignment of our setup, the magnetic field could not be strictly coplanar with our sample plane, leaving a perpendicular component $\Delta H_\perp$ of the field. Thus the obtained Hall resistance is the sum of normal Hall resistance and planar one. Fortunately, the normal Hall resistance is antisymmetric under the opposite magnetic field while the planar Hall resistance is generated by the topological chiral-anomaly term and does not follow the antisymmetry rule under the opposite field [8,9]. As shown in Figs. 2(c) and 2(d), we can exclude the interference of the normal Hall effect by calculating the average data:

$$R_{xy}^{sym} = [R_{xy}(B) + R_{xy}(-B)]/2. \tag{1}$$

Figures 2(e) and 2(f) show the angle-dependent average Hall resistance under $H = 8.5\,\mathrm{T}$ at $T = 10$ and 200 K. However, the average data could not strictly follow the theoretical model [8,9]:

$$\rho_{xy}^{\mathrm{PHE}} = -\Delta\rho_{\mathrm{chiral}} \sin\theta\, \cos\theta, \tag{2}$$

where $\Delta\rho_{\mathrm{chiral}} = \rho_\perp - \rho_\parallel$ gives the anisotropy in resistivity due to the chiral anomaly. $\rho_\perp$ and $\rho_\parallel$ represent the resistivity for magnetic fields applied perpendicular and parallel to the current direction. Although we have subtracted the normal Hall resistance, the Hall configuration misalignment will induce a small component of the in-plane anisotropic magnetoresistance (AMR) and longitudinal offset. As the theoretical works indicated, the AMR displays $\cos^2\theta$ tendency [11,12]. Thus we can fit the data by considering the small contribution of AMR [8,9]:

$$R_{xy}^{sym} = -a\, \sin\theta \cos\theta + b\cos^2\theta + c, \tag{3}$$

where the first part represents the intrinsic PHE and the second and third parts are attributed to the misalignment of the Hall configuration. By using Eq. (3), we can fit the average planar Hall resistance well and display the fitting results in Figs. 2(e)

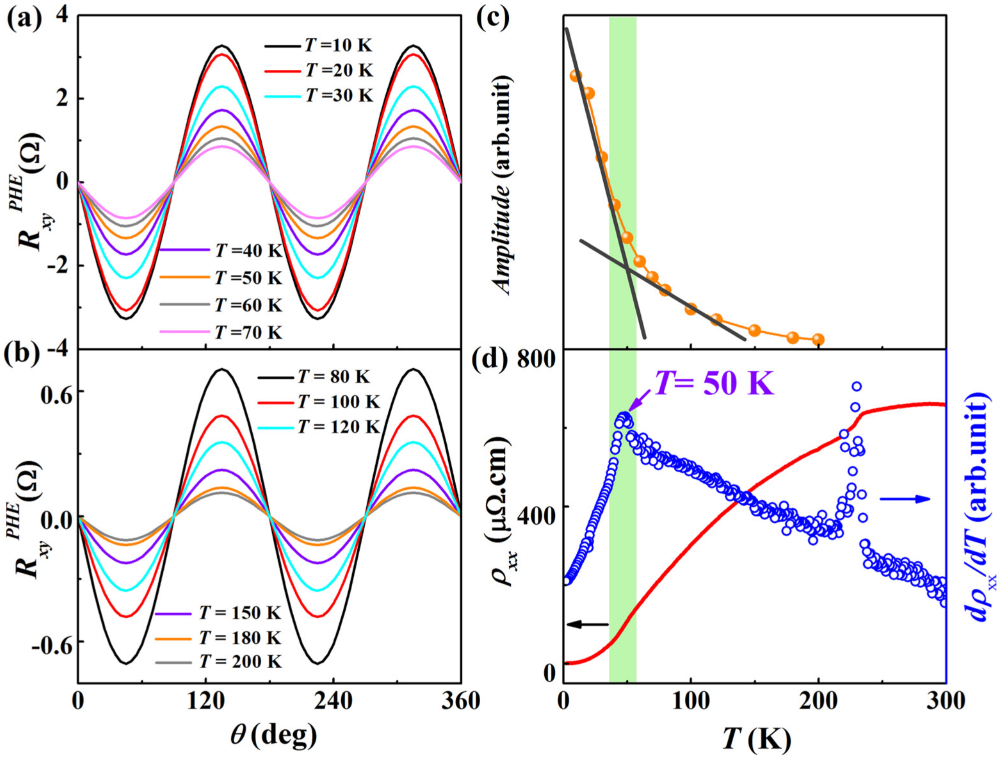

FIG. 3. (a) and (b) The extracted intrinsic planar Hall resistance versus θ at $H = 8.5\,\mathrm{T}$ under various temperatures. (c) The amplitude of PHE versus temperature at $H = 8.5\,\mathrm{T}$. (d) ρ_{xx} and $d\rho_{xx}/dT$ as a function of temperature.

and 2(f). As shown in Figs. 2(g) and 2(h), the intrinsic PHE can be plotted as

$$R_{xy}^{\mathrm{PHE}} = -a\ \sin\theta \cos\theta, \tag{4}$$

where the parameter a, the amplitude of the PHE, was extracted from the fitting results. Having identified the accuracy of our modified fitting model, we subsequently investigate the evolution of amplitude of intrinsic PHE in T_d-MoTe$_2$ with decreasing temperature. We measured the angular dependence of planar Hall resistance at various temperatures under $H = \pm 8.5\,\mathrm{T}$. After fitting the average Hall resistance by using our modified model (the angular dependence of average Hall resistance and fitting results were shown in Supplemental Material Fig. S1), we presented the intrinsic PHE curves at various temperatures in Figs. 3(a) and 3(b). The PHE curves demonstrate a monotonic decrease behavior with the increasing temperature, which is similar to the cases in some Dirac semimetals and WSMs [10,11]. The amplitudes of PHE versus temperature are shown in Fig. 3(c), where a remarkable upturn of the PHE amplitude occurs near ∼50 K. This turning point temperature was reminiscent of the change in the electronic structure around ∼50 K [17]. The previous magnetotransport study demonstrated significant change in the carrier ratio and the thermopower measurement indicated the change of the density of state around ∼50 K [17,29–32]. Moreover, as shown in Fig. 3(d), the $\rho_{xx}(T)$ curve shows abnormal behavior around ∼50 K while the $d\rho_{xx}(T)/dT$ curve shows a broad peak near this temperature, which is corresponding to the possible electronic structure changing in T_d-MoTe$_2$ [17,29].

The onset of anomaly in the PHE amplitudes motivates us to further investigate the field dependence of PHE amplitudes. We have demonstrated the angular dependence of the average PHE under different magnetic field at $T = 10$, 60, and 100 K in Figs. 4(a)–4(c). The amplitudes of PHE versus H at selected temperatures are shown in Figs. 4(d)–4(f). It turns out that the amplitudes of PHE do not behave as similar field dependence above or below $T = 50\,\mathrm{K}$, at which the electronic structure of T_d-MoTe$_2$ undergoes transition and the amplitudes start to increase significantly. As shown in Figs. 4(d)–4(f), the amplitudes of PHE follow a quadratic field dependence behavior at $T = 60$ and 100 K. As indicated in the theoretical work, for the weak magnetic-field limit ($L_a \gg L_c$), the amplitude of PHE follows the relationship [8,9]

$$R_{xy}^{\mathrm{PHE}} \propto (L_c/L_a)^2 \sin\theta \cos\theta, \tag{5}$$

where $L_a = D/\Gamma B$ represents the magnetic-field-induced length scale with D the diffusion coefficient and Γ the transport coefficient. $L_c = (D\tau_c)^{1/2}$ is the chiral charge diffusion length with τ_c the scattering time of chiral charge. To be noteworthy, this field-induced length scale $1/L_a$ quantifies the strength of the chiral-anomaly-induced coupling between the trivial electric and chiral charge. Significant change occurs when the temperature decreases below $T = 50\,\mathrm{K}$. As shown in Fig. 4(d) the fitting curves according to the quadratic law $\sim H^2$ could not match the experiment result. However, it can be divided into two parts: for low fields ($H \leqslant 4\,\mathrm{T}$), the amplitudes depend on H^2; at higher field ($H \geqslant 4\,\mathrm{T}$), the amplitudes show linear variation with field. Indeed, theoretical prediction demonstrated that, in the strong magnetic-field regime $L_a < L_x < L_c^2/L_a$ (L_x is the sample length), the amplitudes of PHE follow the

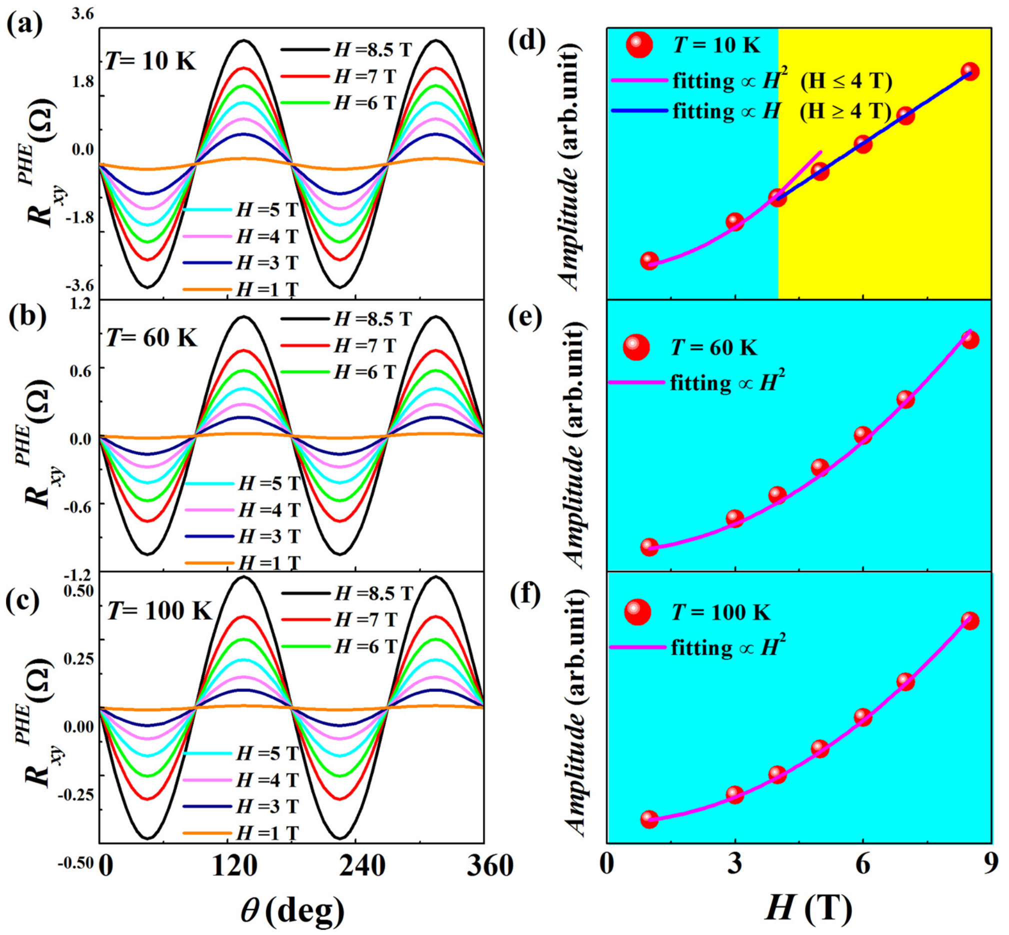

FIG. 4. (a) The extracted intrinsic planar Hall resistance versus θ at $T = 10\,\mathrm{K}$ under various fields. (b) The extracted intrinsic planar Hall resistance versus θ at $T = 60\,\mathrm{K}$ under various fields. (c) The extracted intrinsic planar Hall resistance versus θ at $T = 100\,\mathrm{K}$ under various fields. (d) Magnetic-field dependence of the amplitudes of PHE at $T = 10\,\mathrm{K}$. This can be divided into two regions. The pink and blue lines represent the fitting curves follow quadratic ($H \leqslant 4\,\mathrm{T}$) and linear ($H \geqslant 4\,\mathrm{T}$) dependence, respectively. (d) and (e) Magnetic-field dependence of the amplitudes of PHE at $T = 60$ and 100 K. The pink lines represent the fitting curves follow quadratic dependence.

relationship [8,9,12]:

$$R_{xy}^{\mathrm{PHE}} \propto L_a/L_x \sin\theta \cos\theta. \tag{6}$$

Thus we try to extract the possible origin of the different variation law at the temperatures below/above ~50 K. There is no structural transition reported at $T = 50\,\mathrm{K}$ for T_d-MoTe$_2$. Note that $1/L_a$ describes the coupling strength between the trivial electric and chiral charge. Our previous works indicated the topology of the electron pockets is nearly unchanged while the Fermi level will slightly cross the flat holes band as the temperature decreases below ~50 K. According to the usual Hall resistivity measurements, the density of holes changes significantly around $T \sim 50\,\mathrm{K}$ [32]. Mass anisotropy also shows a sudden upturn around this temperature. The STS dI/dV spectra (proportional to the density of states) demonstrated that the electronic structure of T_d-MoTe$_2$ may not be sensitive to the applied magnetic field at low temperatures [32]. More recently, theoretical works indicated even a small difference of the lattice constant will change the topology of the FS and surface Fermi arc [20,21]. In particular, the flat holes band, lying slightly above the Fermi level, is susceptible to the tuning parameter [17,32]. As the temperature decreases, the chemical potential will slightly move downward and then significantly changes the holes pockets and carrier concentration. The temperature-induced reconstruction of the FS is indeed observed, mainly originating from the holes pockets [17,29]. Meanwhile, all kinds of unusual transport phenomena occurring at the FS evolution temperature point have also been reported. The abnormal Te-Mo coordinate structure at lower temperature has been detected through the temperature-dependent STM measurements [32]. The temperature-dependent spin photocurrent, ratio of electron and holes concentration, and the thermoelectric power also demonstrated anomalies at $T = 50\,\mathrm{K}$ [17,29–32]. Therefore, we could conclude that the FS reconstruction at $T = 50\,\mathrm{K}$, where the trivial electric charge abruptly enhanced, starts to catalyze the strong coupling between the trivial electric and nontrivial chiral charge [17,30]. The FS evolution along with the enhanced carrier density may be fruitful for the coupling effect. The temperature-dependent amplitude of PHE not only reflects the change of the coupling strength with decreasing temperature but also reveals the possible electronic structure transition in this system [8,9]. Besides the drastic enhancement of the amplitude of PHE below the electronic structure evolution temperature, this electronic reconstruction also drives the system into intermediate-coupling state with the help of higher magnetic field ($4\,\mathrm{T} \leqslant H \leqslant 8.5\,\mathrm{T}$) at $T = 10\,\mathrm{K}$ while the system still lies in the weak-coupling state in $H \leqslant 8.5\,\mathrm{T}$ at $T = 60$ and 100 K. Thus the electronic reconstruction also plays a crucial role in the amplification of the chiral charge feature.

In summary, we observe pronounced signature of nontrivial Berry-curvature-induced PHE in type-II WSM candidate T_d-MoTe$_2$. The PHE observed in nonmagnetic T_d-MoTe$_2$ is much stronger and has opposite sign to the case in ferromagnetic metals, which is induced by spin-orbit interactions. This chiral-charge-induced transverse conductance is robust and still visible at $T = 200\,\mathrm{K}$. In particular, we demonstrated temperature-induced variation of the amplitudes of PHE. We showed that an abrupt upturn occurs at $T = 50\,\mathrm{K}$, in which FS reconstruction strengthens the coupling between the electric and chiral charge. Due to the FS reconstruction-induced amplification effect, T_d-MoTe$_2$ can be driven into intermediate-coupling state in higher magnetic field at $T = 10\,\mathrm{K}$. Therefore, our work provides another transport tool to determine chiral fermions in T_d-MoTe$_2$. Due to the numerous transport anomalies that emerge at $T = 50\,\mathrm{K}$ in this system, manipulation of this system through external high pressure or internal chemical pressure could give a comprehensive understanding of their strong-coupling state.

This work was supported by the National Key Research and Development Program under Contracts No. 2016YFA0300404 and No. 2016YFA0401803, the Joint Funds of the National Natural Science Foundation of China and the Chinese Academy of Sciences' Large-Scale Scientific Facility under Contract No. U1432139, the National Nature Science Foundation of China under Contracts No. 11674326 and No. 11774351, the Key Research Program of Frontier Sciences, CAS (QYZDB-SSW-SLH015), and the Anhui Provincial Natural Science Foundation under Contract No. 1708085QA18.

[1] B. Q. Lv, H. M. Weng, B. B. Fu, X. P. Wang, H. Miao, J. Ma, P. Richard, X. C. Huang, L. X. Zhao, G. F. Chen, Z. Fang, X. Dai, T. Qian, and H. Ding, Phys. Rev. X **5**, 031013 (2015).

[2] S. Y. Xu, I. Belopolski, N. Alidoust, M. Neupane, G. Bian, C. Zhang, R. Sankar, G. Chang, Z. Yuan, C. C. Lee, S. Huang, H. Zheng, J. Ma, D. S. Sanchez, B. Wang, A. Bansil, F. Chou, P. P. Shibayev, H. Lin, S. Jia, and M. Z. Hasan, Science **349**, 613 (2015).

[3] K. Deng, G. Wan, P. Deng, K. Zhang, S. Ding, E. Wang, M. Yan, H. Huang, H. Zhang, Z. Xu, J. Denlinger, A. Fedorov, H. Yang, W. Duan, H. Yao, Y. Wu, S. Fan, H. Zhang, X. Chen, and S. Zhou, Nat. Phys. **12**, 1105 (2016).

[4] L. Huang, T. M. McCormick, M. Ochi, Z. Zhao, M. T. Suzuki, R. Arita, Y. Wu, D. Mou, H. Cao, J. Yan, N. Trivedi, and A. Kaminski, Nat. Mater. **15**, 1155 (2016).

[5] J. Jiang, Z. K. Liu, Y. Sun, H. F. Yang, C. R. Rajamathi, Y. P. Qi, L. X. Yang, C. Chen, H. Peng, C. C. Hwang, S. Z. Sun, S. K. Mo, I. Vobornik, J. Fujii, S. S. P. Parkin, C. Felser, B. H. Yan, and Y. L. Chen, Nat. Commun. **8**, 13973 (2017).

[6] C. L. Zhang, S. Y. Xu, I. Belopolski, Z. Yuan, Z. Lin, B. Tong, G. Bian, N. Alidoust, C. C. Lee, S. M. Huang, T. R. Chang, G. Chang, C. H. Hsu, H. T. Jeng, M. Neupane, D. S. Sanchez, H. Zheng, J. Wang, H. Lin, C. Zhang, H. Z. Lu, S. Q. Shen, T. Neupert, M. Zahid Hasan, and S. Jia, Nat. Commun. **7**, 10735 (2016).

[7] Y. Y. Lv, X. Li, B. B. Zhang, W. Y. Deng, S. H. Yao, Y. B. Chen, J. Zhou, S. T. Zhang, M. H. Lu, L. Zhang, M. Tian, L. Sheng, and Y. F. Chen, Phys. Rev. Lett. **118**, 096603 (2017).

[8] A. A. Burkov, Phys. Rev. B **96**, 041110 (2017).

[9] S. Nandy, G. Sharma, A. Taraphder, and S. Tewari, Phys. Rev. Lett. **119**, 176804 (2017).

[10] M. Wu, G. Zheng, W. Chu, W. Gao, H. Zhang, J. Lu, Y. Han, J. Yang, H. Du, W. Ning, Y. H. Zhang, and M. L. Tian, arXiv:1710.01855.

[11] H. Li, H. Wang, H. He, J. Wang, and S. Q. Shen, Phys. Rev. B **97**, 201110 (2018).

[12] P. Li, C. H. Zhang, J. W. Wang, Y. Wen, and X. X. Zhang, arXiv:1803.01213.

[13] H. Yang, S. W. Kim, M. Chhowalla, and Y. H. Lee, Nat. Phys. **13**, 931 (2017).

[14] D. H. Keum, S. Cho, J. H. Kim, D. H. Choe, H. J. Sung, M. Kan, H. Kang, J. Y. Hwang, S. W. Kim, H. Yang, K. J. Chang, and Y. H. Lee, Nat. Phys. **11**, 482 (2015).

[15] Y. Wang, J. Xiao, H. Zhu, Y. Li, Y. Alsaid, K. Y. Fong, Y. Zhou, S. Wang, W. Shi, Y. Wang, A. Zettl, E. J. Reed, and X. Zhang, Nature (London) **550**, 487 (2017).

[16] R. He, S. Z. Zhong, H. H. Kim, G. H. Ye, Z. P. Ye, L. Winford, D. McHaffie, I. Rilak, F. C. Chen, X. Luo, Y. P. Sun, and Adam W. Tsen, Phys. Rev. B **97**, 041410 (2018).

[17] F. C. Chen, H. Y. Lv, X. Luo, W. J. Lu, Q. L. Pei, G. T. Lin, Y. Y. Han, X. B. Zhu, W. H. Song, and Y. P. Sun, Phys. Rev. B **94**, 235154 (2016).

[18] Y. Qi, P. G. Naumov, M. N. Ali, C. R. Rajamathi, W. Schnelle, O. Barkalov, M. Hanfland, S. C. Wu, C. Shekhar, Y. Sun, V. Suss, M. Schmidt, U. Schwarz, E. Pippel, P. Werner, R. Hillebrand, T. Forster, E. Kampert, S. Parkin, R. J. Cava, C. Felser, B. Yan, and S. A. Medvedev, Nat. Commun. **7**, 11038 (2016).

[19] F. C. Chen, X. Luo, R. C. Xiao, W. J. Lu, B. Zhang, H. X. Yang, J. Q. Li, Q. L. Pei, D. F. Shao, R. R. Zhang, L. S. Ling, C. Y. Xi, W. H. Song, and Y. P. Sun, Appl. Phys. Lett. **108**, 162601 (2016).

[20] Y. Sun, S. C. Wu, M. N. Ali, C. Felser, and B. Yan, Phys. Rev. B **92**, 161107 (2015).

[21] Z. Wang, D. Gresch, A. A. Soluyanov, W. Xie, S. Kushwaha, X. Dai, M. Troyer, R. J. Cava, and B. A. Bernevig, Phys. Rev. Lett. **117**, 056805 (2016).

[22] P. Deng, Z. Xu, K. Deng, K. Zhang, Y. Wu, H. Zhang, S. Zhou, and X. Chen, Phys. Rev. B **95**, 245110 (2017).

[23] X. Huang, L. Zhao, Y. Long, P. Wang, D. Chen, Z. Yang, H. Liang, M. Xue, H. Weng, Z. Fang, X. Dai, and G. Chen, Phys. Rev. X **5**, 031023 (2015).

[24] P. Goswami, J. H. Pixley, and S. Das Sarma, Phys. Rev. B **92**, 075205 (2015).

[25] F. Arnold, C. Shekhar, S. C. Wu, Y. Sun, R. D. dos Reis, N. Kumar, M. Naumann, M. O. Ajeesh, M. Schmidt, A. G. Grushin, J. H. Bardarson, M. Baenitz, D. Sokolov, H. Borrmann, M. Nicklas, C. Felser, E. Hassinger, and B. Yan, Nat. Commun. **7**, 11615 (2016).

[26] See Supplemental Material at http://link.aps.org/supplemental/10.1103/PhysRevB.98.041114 for experiment details of sample preparation, calculated details, the geometry of the samples and electrodes and the anisotropic magnetoresistance.

[27] Z. J. Xiang, G. J. Ye, C. Shang, B. Lei, N. Z. Wang, K. S. Yang, D. Y. Liu, F. B. Meng, X. G. Luo, L. J. Zou, Z. Sun, Y. Zhang, and X. H. Chen, Phys. Rev. Lett. **115**, 186403 (2015).

[28] J. Hu, Z. Tang, J. Liu, X. Liu, Y. Zhu, D. Graf, K. Myhro, S. Tran, C. N. Lau, J. Wei, and Z. Mao, Phys. Rev. Lett. **117**, 016602 (2016).

[29] Q. Zhou, D. Rhodes, Q. R. Zhang, S. Tang, R. Schönemann, and L. Balicas, Phys. Rev. B **94**, 121101 (2016).

[30] Y. Wu, N. H. Jo, M. Ochi, L. Huang, D. Mou, S. L. Bud'ko, P. C. Canfield, N. Trivedi, R. Arita, and A. Kaminski, Phys. Rev. Lett. **115**, 166602 (2015).

[31] S. Lim, C. R. Rajamathi, V. Süß, C. Felser, and A. Kapitulnik, arXiv:1802.02838.

[32] Q. L. Pei, W. J. Meng, X. Luo, H. Y. Lv, F. C. Chen, W. J. Lu, Y. Y. Han, P. Tong, W. H. Song, Y. B. Hou, Q. Y. Lu, and Y. P. Sun, Phys. Rev. B **96**, 075132 (2017).